Computational aspects of guided wave based damage localization algorithms in flat anisotropic structures

Jochen Moll*[1], Miguel Angel Torres-Arredondo[2] and Claus-Peter Fritzen[2]

[1]*Goethe University of Frankfurt, Department of Physics, Terahertz Photonics Group,
Max-von-Laue-Strasse 1, 60438 Frankfurt am Main, Germany*
[2]*University of Siegen, Institute of Mechanics and Control Engineering – Mechatronics,
Paul-Bonatz-Straße 9-11, 57076 Siegen, Germany*

Abstract. Guided waves have shown a great potential for structural health monitoring (SHM) applications. In contrast to traditional non-destructive testing (NDT) methodologies, a key element of SHM approaches is the high process of automation. The monitoring system should decide autonomously whether the host structure is intact or not. A basic requirement for the realization of such a system is that the sensors are permanently installed on the host structure. Thus, baseline measurements become available that can be used for diagnostic purposes, i.e., damage detection, localization, etc. This paper contributes to guided wave-based inspection in anisotropic materials for SHM purposes. Therefore, computational strategies are described for both, the solution of the complex equations for wave propagation analysis in composite materials based on exact elasticity theory and the popular global matrix method, as well as the underlying equations of two active damage localization algorithms for anisotropic structures. The result of the global matrix method is an angular and frequency dependent wave velocity characteristic that is used subsequently in the localization procedures. Numerical simulations and experimental investigations through time-delay measurements are carried out in order to validate the proposed theoretical model. An exemplary case study including the calculation of dispersion curves and damage localization is conducted on an exemplary unidirectional composite structure where the ultrasonic signals processed in the localization step are simulated with the spectral element method. The proposed study demonstrates the capabilities of the proposed algorithms for accurate damage localization in anisotropic structures.

1. Introduction

Guided ultrasonic waves have many useful properties that can be exploited for the health monitoring of mechanical structures. Hence, acoustic emission (AE) and ultrasonic testing (UT) make use of these high frequency waves. These techniques receive a lot of attention for such advantages as low cost, highly automated operation and high sensitivity for flaw detection as well as material characterization and manufacturing control. These attributes make these techniques a valuable tool in order to get information regarding the origin and importance of a discontinuity in a structure for a longer safe life and lower operation costs (Staszewski *et al*. 2004).

---

*Corresponding author, Dr., E-mail: moll@physik.uni-frankfurt.de, http://www.jochenmoll.de

Guided ultrasonic waves, actively excited by means of piezoelectric or piezocomposite transducers, or associated with stress waves generated by mechanical deformation of a material, have shown great potential for identifying structural defects in isotropic and anisotropic plate-like structures. Depending on the material attenuation and geometric beamspreading effects, guided waves are able to propagate over relative long distances, interact sensitively with and/or being related to different types of defects like e.g., delaminations (Hayashi and Kawashima 2002), corrosion damage (Yu *et al.* 2008), etc. However, it is only possible to benefit from these advantages once the complexity of guided wave propagation is disclosed. In the framework of structural health monitoring (SHM), the transducers are permanently installed on or embedded into the structure so that baseline measurements become available that can be used for diagnostic and analysis purposes, i.e., damage detection, localization, source mechanism characterization, etc.

State-of-the-art active localization methodologies often assume that the wave velocity of the ultrasonic waves is constant for a particular frequency-thickness product and does not depend on the direction of propagation. This hypothesis holds for quasi-isotropic materials, where the multilayered and multioriented composition of the structure mitigates the anisotropic impact of each layer. On the contrary, this assumption breaks down in case of a general anisotropic material where the velocity and energy of propagation of the multiple modes are both frequency and angular dependent. In order to avoid a systematic error coming from the isotropy assumption, new damage localization methodologies are needed that incorporate the anisotropic material properties of the structure via a directional wave velocity characteristic. Generally, there are two ways to obtain such a velocity characteristic. The first strategy uses the material constants measured by means of different inversion or material testing techniques. They are then fed into an analytic or finite element model to extract the relevant information (Castaings *et al.* 2000, Barkanov *et al.* 2007, Calomfirescu and Herrmann 2007). A second approach is based on experimental time-delay measurements as they are performed in (Hartmann *et al.* 2010, Moll *et al.* 2010).

In this paper, guided ultrasonic waves generated by piezoelectric transducers on a composite plate are studied for damage localization. For the theoretical analysis, an exact three dimensional model is employed and prefered over common plate theories. This motivation is given by the fact that plate theories only provide results with an admissible accuracy in the low frequency range and for the case of a relatively simple complexity of the structure (Torres-Arredondo and Fritzen 2011). By increasing the complexity of the structure, i.e., as the number of constitutive layers increases, the solutions obtained with the plate theories start to highly deviate from the exact solutions and render to incorrect results. Moreover, plate theories require the calculation of correction factors in order to match frequencies from the approximate theory to frequencies obtained from the exact theory. For the general case of a laminate, this procedure becomes burdensome as the value of the correction factors depends on the number, stacking sequence and properties of the constitutive plies (Whitney and Sun 1973). Although many modeling attempts are presented in the literature, only few describe in detail the numerical implementation to solve the underlying complex equations provided by the exact elasticity theory (Wang and Yuan 2007). Hence, the first goal of this paper is to present a robust and automatic guideline for the implementation of the solutions given by the proposed theory based on the global matrix method in section 2. The development of the characteristic equations is presented and dispersion relations are obtained from them. Another major part focuses on two algorithms that provide autonomous damage localization in anisotropic materials. Therefore, section 3 introduces both algorithms mathematically and describes numerical issues for the respective implementation. Additionally, this part contains a discussion of the individual algorithmic properties.

Results for damage localization in a unidirectional composite structure are presented in section 4 using the theoretically calculated group velocities from the global matrix method.

2. Global matrix method

The modeling of wave propagation in multilayered anisotropic structures has been extensively studied by several researchers and a considerable amount of literature has been published on this topic (Mal 1988, Rose 1999, Kundu 2004). Analyzing guided waves in these structures is often categorized into three methods. There are methods based on three dimensional elasticity, laminated plate theories of different orders and waveguide finite element methods. For completeness, the modeling and solution of wave propagation problems in anisotropic materials is discussed in this section. In addition, the importance of the angular and frequency dependency of the group velocity is discussed due to its high relevance in damage and impact localization as well as mode recognition routines. The first part of this section shows an extended mathematical model from the formulation introduced by Nayfeh in his original paper (Nayfeh 1991). In the second part, the proposed method is validated with experimental measurements for two different anisotropic structures; a unidirectional glass fibre reinforced plastic (GFRP) plate with a relatively strong degree of anisotropy and a multilayered quasi-isotropic carbon fibre reinforced plastic (CFRP) structure.

2.1 Lamb wave propagation solution in composite materials

Lamb waves in plate-like structures result from the superposition of guided longitudinal and transverse shear waves within a layer. There exist two groups of waves, whose particle motion is either symmetric or antisymmetric about the mid-plane of the plate, and each can propagate independently of the other. A common approach for the wave propagation modeling in composite materials is to consider a flat, linearly elastic, non-piezoelectric layer of material possessing a monoclinic crystal symmetry subjected to a complex stress system in three dimensions. A global Cartesian coordinate system (x_1, x_2, x_3) is assumed with the x_3-axis normal to the mid-plane of the layer with outer surfaces at $x_3 = \pm h/2$, where h denotes the thickness of the layer as depicted in Fig. 1. The governing equations of motion in the absence of body forces are given by
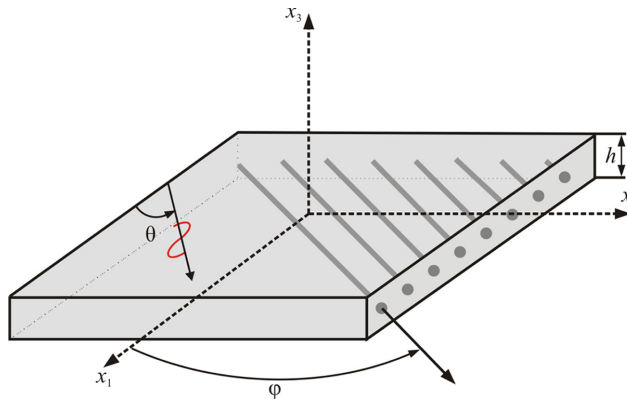

Fig. 1 Lamb wave propagation in the global coordinate system

$$\frac{\partial \sigma_{ij}}{\partial x_j} = \rho \frac{\partial^2 u_i}{\partial t^2} \tag{1}$$

where indices *i* and *j* vary over 1,2,3, ρ denotes the material density, σ_{11}, σ_{12}, ..., the stress components acting on the faces of the material, and *u* the displacement vector in the x_1, x_2 and x_3 global coordinate system. The usual summation convention over repeated subscripts is assumed. The constitutive relations showing the interdependence of strain and stress are defined in terms of the stiffness matrix $C_{pq}(p,q=1,2,\ldots,6)$ as given in Eq. (2)

$$\begin{bmatrix} \sigma_{11} \\ \sigma_{22} \\ \sigma_{33} \\ \sigma_{23} \\ \sigma_{13} \\ \sigma_{12} \end{bmatrix} = \begin{bmatrix} C_{11} & C_{12} & C_{13} & 0 & 0 & C_{16} \\ C_{12} & C_{22} & C_{23} & 0 & 0 & C_{26} \\ C_{13} & C_{23} & C_{33} & 0 & 0 & C_{36} \\ 0 & 0 & 0 & C_{44} & C_{45} & 0 \\ 0 & 0 & 0 & C_{45} & C_{55} & 0 \\ C_{16} & C_{26} & C_{36} & 0 & 0 & C_{66} \end{bmatrix} \begin{bmatrix} \varepsilon_{11} \\ \varepsilon_{22} \\ \varepsilon_{33} \\ \varepsilon_{23} \\ \varepsilon_{13} \\ \varepsilon_{12} \end{bmatrix} \tag{2}$$

Viscoelastic layers can be simulated by allowing the stiffness matrix to be complex (Szabo and Wu 2000). If the global coordinate system does not coincide with the material coordinate system, but is rotated by an angle φ around the x_3-axis, a coordinate transformation of the elastic stiffness matrix is required so that the axes of the anisotropic medium coincide with the chosen global coordinate axes (Vasiliev and Morozov 2007). The linear strain-displacement relations are defined in accordance to (Hearn 1977) as

$$\varepsilon_{k1} = \frac{1}{2}\left(\frac{\partial u_1}{\partial x_k} + \frac{\partial u_k}{\partial x_1}\right) \tag{3}$$

where indices *k* and *l* vary over 1,2,3. Formal solutions for the three displacement equations are sought in the complex plane in the following form (Nayfeh 1995)

$$(u_1,u_2,u_3) = (U_1,U_2,-iU_3)e^{ik(x_1\cos(\theta)+x_2\sin(\theta)+px_3-c_{ph}t)} \tag{4}$$

where *k* is the wavenumber, θ the angle of propagation, *p* is an unknown parameter, c_{ph} is the phase velocity defined as $c_{ph}=\omega/k$, ω is the angular frequency and *U* is the displacement amplitude vector defining the polarization. The complete solution to the problem, including the relevant equations, is presented in Appendix A.

Once the expressions for displacement and stress fields have been defined (see Appendix A), boundary and continuity conditions can be imposed at each interface and free surface of the medium. The number and type of conditions depend on the layer and surface type, i.e., solid, liquid or vacuum. At the free surfaces, the stress components are required to vanish. In the case of a single layered system, the boundary conditions are then imposed on the upper and lower surfaces of the same layer. For a multilayered system, under the assumption of perfectly bonded layers, the field components of the layers above and below the interface are specified as equal. There are two

$$
\boldsymbol{P} = \boldsymbol{K}_{global}\boldsymbol{U} =
\overbrace{\phantom{K^-_{12}\ K^-_{14}\ K^-_{16}}}^{\text{Free surface 1}}\
\overbrace{\phantom{-K^+_{11}\ -K^+_{12}\ -K^+_{13}\ -K^+_{14}\ -K^+_{15}\ -K^+_{16}}}^{\text{Layer 1}}\
\overbrace{\phantom{-K^+_{11}\ -K^+_{12}\ -K^+_{13}\ -K^+_{14}\ -K^+_{15}\ -K^+_{16}}}^{\text{Layer 2}}\
\overbrace{\phantom{-K^+_{11}\ -K^+_{13}\ -K^+_{15}}}^{\text{Free surface 2}}
$$

$$
\begin{pmatrix}
K^-_{12} & K^-_{14} & K^-_{16} & -K^+_{11} & -K^+_{12} & -K^+_{13} & -K^+_{14} & -K^+_{15} & -K^+_{16} & & & & & & & & & & & \\
K^-_{22} & K^-_{24} & K^-_{26} & -K^+_{21} & -K^+_{22} & -K^+_{23} & -K^+_{24} & -K^+_{25} & -K^+_{26} & & & & & & & & & & & \\
K^-_{32} & K^-_{34} & K^-_{36} & -K^+_{31} & -K^+_{32} & -K^+_{33} & -K^+_{34} & -K^+_{35} & -K^+_{36} & & & & & & & & & & & \\
K^-_{42} & K^-_{44} & K^-_{46} & -K^+_{41} & -K^+_{42} & -K^+_{43} & -K^+_{44} & -K^+_{45} & -K^+_{46} & & & & & & & & & & & \\
K^-_{52} & K^-_{54} & K^-_{56} & -K^+_{51} & -K^+_{52} & -K^+_{53} & -K^+_{54} & -K^+_{55} & -K^+_{56} & & & & & & & & & & & \\
K^-_{62} & K^-_{64} & K^-_{66} & -K^+_{61} & -K^+_{62} & -K^+_{63} & -K^+_{64} & -K^+_{65} & -K^+_{66} & & & & & & & & & & & \\
 & & & K^-_{11} & K^-_{12} & K^-_{13} & K^-_{14} & K^-_{15} & K^-_{16} & -K^+_{11} & -K^+_{12} & -K^+_{13} & -K^+_{14} & -K^+_{15} & -K^+_{16} & & & & & \\
 & & & K^-_{21} & K^-_{22} & K^-_{23} & K^-_{24} & K^-_{25} & K^-_{26} & -K^+_{21} & -K^+_{22} & -K^+_{23} & -K^+_{24} & -K^+_{25} & -K^+_{26} & & & & & \\
 & & & K^-_{31} & K^-_{32} & K^-_{33} & K^-_{34} & K^-_{35} & K^-_{36} & -K^+_{31} & -K^+_{32} & -K^+_{33} & -K^+_{34} & -K^+_{35} & -K^+_{36} & & & & & \\
 & & & K^-_{41} & K^-_{42} & K^-_{43} & K^-_{44} & K^-_{45} & K^-_{46} & -K^+_{41} & -K^+_{42} & -K^+_{43} & -K^+_{44} & -K^+_{45} & -K^+_{46} & & & & & \\
 & & & K^-_{51} & K^-_{52} & K^-_{53} & K^-_{54} & K^-_{55} & K^-_{56} & -K^+_{51} & -K^+_{52} & -K^+_{53} & -K^+_{54} & -K^+_{55} & -K^+_{56} & & & & & \\
 & & & K^-_{61} & K^-_{62} & K^-_{63} & K^-_{64} & K^-_{65} & K^-_{66} & -K^+_{61} & -K^+_{62} & -K^+_{63} & -K^+_{64} & -K^+_{65} & -K^+_{66} & & & & & \\
 & & & & & & & & & K^-_{11} & K^-_{12} & K^-_{13} & K^-_{14} & K^-_{15} & K^-_{16} & -K^+_{11} & -K^+_{13} & -K^+_{15} \\
 & & & & & & & & & K^-_{21} & K^-_{22} & K^-_{23} & K^-_{24} & K^-_{25} & K^-_{26} & -K^+_{21} & -K^+_{23} & -K^+_{25} \\
 & & & & & & & & & K^-_{31} & K^-_{32} & K^-_{33} & K^-_{34} & K^-_{35} & K^-_{36} & -K^+_{31} & -K^+_{33} & -K^+_{35} \\
 & & & & & & & & & K^-_{41} & K^-_{42} & K^-_{43} & K^-_{44} & K^-_{45} & K^-_{46} & -K^+_{41} & -K^+_{43} & -K^+_{45} \\
 & & & & & & & & & K^-_{51} & K^-_{52} & K^-_{53} & K^-_{54} & K^-_{55} & K^-_{56} & -K^+_{51} & -K^+_{53} & -K^+_{55} \\
 & & & & & & & & & K^-_{61} & K^-_{62} & K^-_{63} & K^-_{64} & K^-_{65} & K^-_{66} & -K^+_{61} & -K^+_{63} & -K^+_{65} \\
\end{pmatrix} \boldsymbol{U}
$$

Fig. 2 Global matrix structure for a two layer case: The matrix is built of submatrices describing the behaviour of the individual layers. The blank spaces are filled zeros. Signs ±) indicate the upper and lower surfaces of the layers. The entries for each position in the matrix can be found according to (31)

popular approaches used in order to solve the wave propagation problem. They are known as the transfer matrix method and the global matrix method (Lowe 1995). In this work the second approach is recommended since it is more robust and remains numerically stable for any frequency-to-thickness product (Mal 1998). Fig. 2 depicts how the global matrix $\boldsymbol{K}_{global}$ is assembled for a two layer system bounded by a solid interface (Pavlakovic 1997). Superscripts refer to the top and bottom conditions for each layer at $x_3 = \pm h/2$, $\boldsymbol{P}$ is the displacement and stress vector, and $\boldsymbol{U}$ is the displacement amplitude vector. The entries for each position in the matrix can be found according to (31).

Once the global matrix is assembled, the dispersion relations are obtained by setting the determinant of the global matrix depicted in Fig. 2 to zero. This can be considered as a characteristic function relating the angular frequency, or phase velocity, to wavenumber for given material properties and propagation direction. A good technique to start the mode tracing procedure is to find roots by scanning the phase velocity at a fixed frequency or the frequency at a fixed velocity as recommended by Lowe (1993). An algorithm based on the golden section search and parabolic interpolation is used here for the root finding procedures. To initialize the search, the minima of the modulus of the determinant of the global matrix are calculated since they correspond to existing solutions. These minima are used as the initial guesses of the solution in the root finding algorithm. Each of the calculated roots is then a mode and a point to start the tracing of a dispersion curve. It should be remarked that sometimes during the scanning procedure the sudden change in the nature, i.e., from pure real roots to complex roots and vice versa, and magnitude of the eigenvalues in Eq. (4) give rise to spurious roots along the wavenumber curve. However, for a given angle of propagation these spurious points are repeated in the whole frequency range and render the same values of velocities, what makes their separation and elimination from true modes to a certain extent easy. This can be

accomplished by scanning the roots at different frequency points and checking the velocity values provided by these roots. Finally, by selecting a particular true wave mode, cubic extrapolation can be used in order to produce the new seed for the tracing algorithm which improves not only the stability of the result, but also the computational time required to trace a mode.

Finally, by tracing the right solution of a mode, and once the phase velocity relations have been calculated, the expression of the group velocity as function of the global matrix determinant can be obtained. The group velocity c_{Gr} is related to the velocity with which the envelope of a wave packet propagates. It is well known that for anisotropic materials the group velocity differs from the phase front direction and its dispersion characteristics are angular and frequency dependent. As demonstrated in Auld (1973), in the case of non-absorbing media, the energy velocity is strictly equal to the group velocity. This is a very valuable characteristic that provides important information for signal analysis due to the fact that the received signal contains the energy information. The group velocity components $c_{Gr,x1}$ and $c_{Gr,x2}$ in the Cartesian coordinate system can be deduced according to the definition given by Auld (1973)

$$c_{Gr} = \sqrt{c_{Gr,x_1}^2 + c_{Gr,x_2}^2}, \quad \vartheta = tan^{-1}\left(\frac{c_{Gr,x_2}}{c_{Gr,x_1}}\right) \tag{5}$$

where

$$c_{Gr,x_1} = \frac{\partial \omega}{\partial k}\cos(\theta) - \frac{\partial \omega}{\partial \theta}\frac{\sin(\theta)}{k} \tag{6}$$

$$c_{Gr,x_2} = \frac{\partial \omega}{\partial k}\sin(\theta) - \frac{\partial \omega}{\partial \theta}\frac{\cos(\theta)}{k} \tag{7}$$

Note that the results obtained in this section apply rigorously only to lossless media. Eqs. (5), (6) and (7) can be solved whether for a fixed propagation angle and variable frequency or a variable angle of propagation and fixed frequency. This leads to the calculation of a group velocity dispersion curve or a wavefront curve, respectively. The first derivative term $\partial \omega/\partial k$ can be computed directly by numerical differentiation of the wavenumber curve, and the second derivative $\partial \omega/\partial \theta$ can be approximated by a finite difference scheme. A central difference is recommended since it yields to a more accurate approximation in comparison to other schemes given by the fact that its error is proportional to the square of the spacing.

2.2 Validation of the theoretical model

The mathematical model and procedures presented in the previous sections were implemented in Matlab. Two different structures are analyzed in the following. First, an approximately 1.5mm thick composite material made of unidirectional glass fibre reinforced plastic (GFRP) with properties listed in Table 1 and shown in Fig. 12 is studied. Dispersion curves for phase and group velocities are depicted in Fig. 3. The analysis in this section will concentrate on the low frequency range which is mostly used in Lamb wave applications for structural health monitoring where just the fundamental modes are present. Thus, the influence of higher order modes of propagation is often avoided in order to facilitate the analysis of the recorded signals. It is well known that the fundamental symmetric S_0 mode is typically used for the identification of cracks, while the fundamental antisymmetric A_0 mode is used for detection of delaminations.

Table 1 Material properties of unidirectional glass fibre reinforced plastic

E_1 (GPa)	E_2 (GPa)	E_3 (GPa)	G_{12} (GPa)	G_{13} (GPa)	G_{23} (GPa)	$v_{12}=v_{13}=v_{23}$	ρ (kg/m³)
7	15.2	10	4	3.1	2.75	0.3	1700

From Fig. 3 it can be seen that the behaviour of the SH_0 and S_0 modes are different from the A_0 mode in both the low and high frequency zones. According to the dispersion curves depicted in Figs. 3(a) and (b), the S_0 and SH_0 modes are almost non-dispersive in the low frequency region while the A_0 mode is highly dispersive. It can also be clearly seen in the low frequency regime that the higher the frequency of the A_0 mode, the faster its group velocity. In an opposite manner for the S_0 and SH_0 modes, the higher their frequency, the slower their group velocity. The results from the velocity and wave curves in Figs. 3(c) and (d) show that the material possesses a high degree of anisotropy. It can also be seen that the mode velocity is strongly related to the frequency and orientation of propagation. This is a common characteristic of anisotropic materials where not only the velocity, but also the attenuation and energy of propagation of the multiple modes are both frequency and angular dependent. It is interesting to notice that the velocity curves can have several inflexion points responsible for the cusps of the associated group velocity. This phenomenon is known as energy focusing. These dispersion characteristics of the fundamental modes of propagation have been studied by the authors in order to distinguish modes of propagation in recorded acoustic emission waveforms for mode identification and source location based on atomic energy distribution analysis (Torres-Arredondo and Fritzen 2011). Additionally, the knowledge of dispersion characteristics
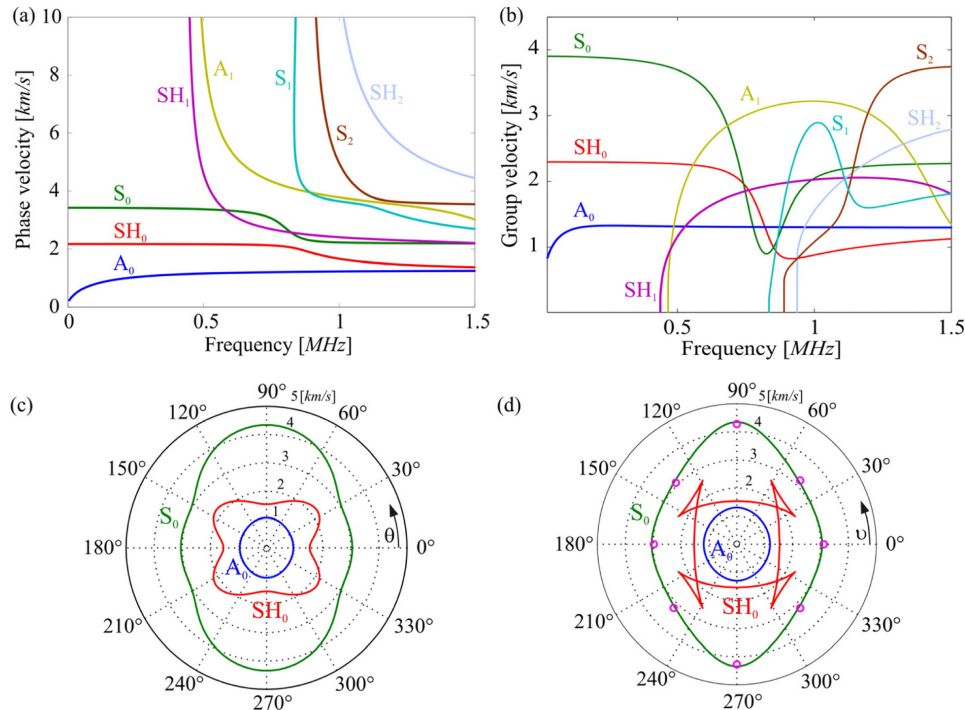

Fig. 3 Dispersion curves for the multilayered CFRP: (a) Phase velocity along θ=45°, (b) group velocity along θ=45°, (c) velocity curve at f=100 kHz and (d) wave curve at f=100 kHz

is crucial in ultrasonic inspection techniques where the selection of the optimal inspection frequencies plays an important role for the improvement of the sensitivity and for optimization of the sensor network in terms of sensor placement and number of sensors.

In order to validate the proposed analytical model with experimental data, the wave surface for the S_0 mode at a central frequency of 100 kHz is shown in comparison with some measured values at discrete angular points (circles in magenta) in Fig. 3(d). The experimental group velocites were determined at the defined frequency by means of time-delay measurements. The experimental setup and transducers placement are depicted in Fig. 12 and discussed in detail in section 4. It can be seen from Fig. 3(d) that the estimated group velocity matches the theoretical curve very well, demonstrating the effectiveness of the model. It is apparent that the proposed model can provide precise estimations of the group velocity. The displacement profiles across the thickness of the composite lamina are depicted for the fundamental A_0 and S_0 modes of propagation in Fig. 4 in order to show the mode shape changing behaviour with frequency. As it can be infered from Fig. 4, in the low frequency range the A_0 and S_0 are mostly pure flexural and extensional modes, respectively. At higher frequencies, the mode shapes for each mode begin to vary and the dominant motions from the low frequency start to decrease while the non-dominant increase on the outside surfaces where the measurements are normally made.

Second, a carbon fibre reinforced plastic (CFRP) with stacking sequence [0 90 -45 45 0 90 -45 45]$_s$ and total thickness of 4.2 mm is analyzed. The nominal material parameters of the unidirectional layers provided by the manufacturer are given in Table 2 (Schulte 2010). Fig. 5(a) shows the plate of approximately 500 mm × 500 mm instrumented with nine piezo electric transducers. The squared piezo patches have a side length of 10 mm and a thickness of 0.5 mm. A 3 cycle tone burst signal with a 60 kHz centre frequency was used as the input waveform. The piezoelectric transducer number five was designated as the actuator. The calculated group velocities at frequency of 60 kHz are depicted in Fig. 5(b) together with experimental data (magenta and black circles). It is shown again that the proposed method provides accurate estimates of velocity. Additionally, it can be also inferred that the mode wave velocities and energy concentration are not strongly related to the
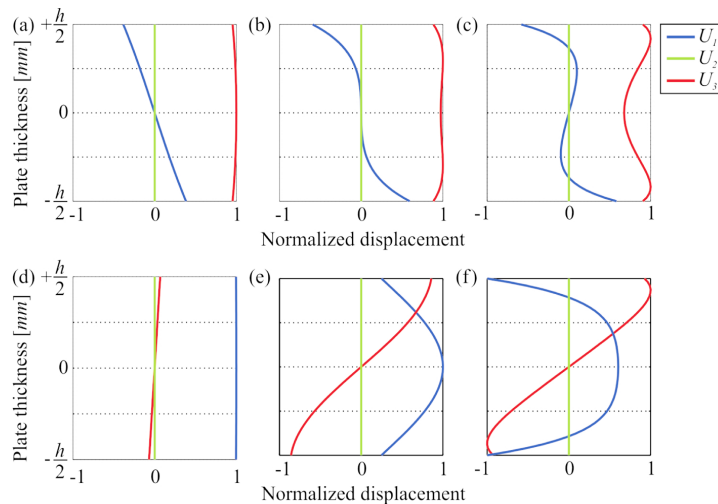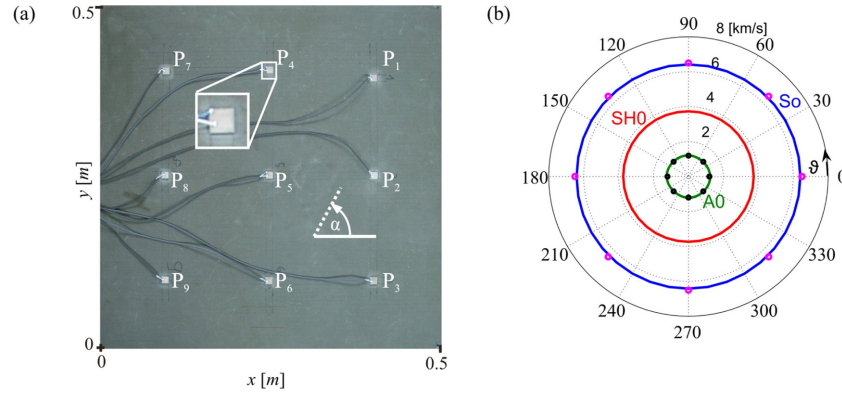

Fig. 4 Mode shapes for fundamental modes of propagation: (a) A_0 at f=150 kHz, (b) A_0 at f=250 kHz, (c) A_0 at f=350 kHz, (d) S_0 at f=150 kHz, (e) S_0 at f=250 kHz and (f) S_0 at f=350 kHz

Table 2 Material properties of carbon fibre reinforced plastic

E_1 (GPa)	E_2 (GPa)	E_3 (GPa)	G_{12} (GPa)	G_{13} (GPa)	G_{23} (GPa)	$\nu_{12}=\nu_{13}=\nu_{23}$	ρ (kg/m³)
155	8.5	8.5	4	4	4	0.33	1600

Fig. 5 Dispersion curves for the multilayered CFRP: (a) Experimental Setup and (b) numerical wave curve at *f*=60 kHz together with experimental measurements

frequency and orientation of propagation. This is given by the fact that the multilayered and multi-oriented composition of the structure mitigates the anisotropic impact of each layer.

3. Damage localization strategies in anisotropic structures

A challenge of damage localization in anisotropic structures is that the group velocity of the fundamental wave modes $c_{Gr}(fd,\theta,EOC)$ is generally a function of the excitation frequency *f*, the thickness of the host structure *d* as well as changing environmental and operation conditions *EOC*. As shown in the previous section, the wave velocity also changes with the direction of propagation θ. In the following part, two localization algorithms will be presented that account for the anisotropic material properties by integrating the known velocity characteristic, e.g., obtained by the theoretical approach from section 2, into their localization formulation. A common property of both algorithms is the fact that they are based on differential signals between measurements of the pristine and the damaged structure. Thus, reflections from structural elements like e.g., boundaries or stiffeners are eliminated. As a result, the first wave packet in the differential signal represents the interaction with the defect. For a practical realization of these methods, the temperature effect must be eliminated. This can be efficiently achieved through a combination of optimal baseline selection (OBS) and baseline signal stretch (BSS). A discussion of the temperature effect and its compensation is documented in (Croxford *et al.* 2010, Clarke *et al.* 2010, Torres-Arredondo and Fritzen 2012, Moll and Fritzen 2012).

Although the mathematical description of both localization formulations is the same, many structural differences exist that should be discussed in the final part of this section. The major difference that has a direct impact on the particular formulation refers to the spatial discretization of the structure. The classical time-of-arrival (TOA) algorithm (Konstantinidis *et al.* 2006, Michaels *et al.* 2008, Ng and Veidt 2009) needs such a spatial sampling, e.g., realized through an equidistant

grid, in order to evaluate the intensity of the resulting damage map at these positions. On the other hand, the anisotropic damage triangulation method does not need this spatial discretization because the underlying transcendental equations can be solved numerically with the knowledge of time-of-flight measurements (Moll *et al.* 2010). In both cases the data acquisition follows a modified common source scheme (Davies *et al.* 2006), where all possible pitch-catch signals are evaluated for damage localization in a spatially distributed sensor network.

3.1 Triangulation method in anisotropic structures

Fig. 6 shows a schematic with a single actuator-sensor pair having the coordinates x_m and x_n. The Euclidean distance between the actuator and the sensor is L. The partial distance $d_{1,o}$ from the actuator to the damage is the travel time of the ultrasonic wave TOF_1 (i.e., time of flight) multiplied with the group velocity c_{Gr} in this direction is

$$d_{1,o} = TOF_1 \cdot c_{Gr}(fd, \theta_1 + \tau, EOC) \tag{8}$$

The other distances can be expressed similarly as

$$d_{2,o} = TOF_2 \cdot c_{Gr}(fd, \pi - \theta_2 + \tau, EOC) \tag{9}$$

$$d_{1,u} = TOF_1 \cdot c_{Gr}(fd, -\theta_1 + \tau, EOC) \tag{10}$$

$$d_{2,u} = TOF_2 \cdot c_{Gr}(fd, \pi + \theta_2 + \tau, EOC) \tag{11}$$

The indices o and u denote the upper and lower triangle of Fig. 6, respectively. Using the law of sines leads to geometric equations for the upper triangle

$$\frac{\sin(\theta_2)}{TOF_1 \cdot c_{Gr}(fd, \theta_1 + \tau, EOC)} = \frac{\sin(\theta_3)}{L} \text{ and } \theta_3 = \pi - \theta_1 - \theta_2 \tag{12}$$
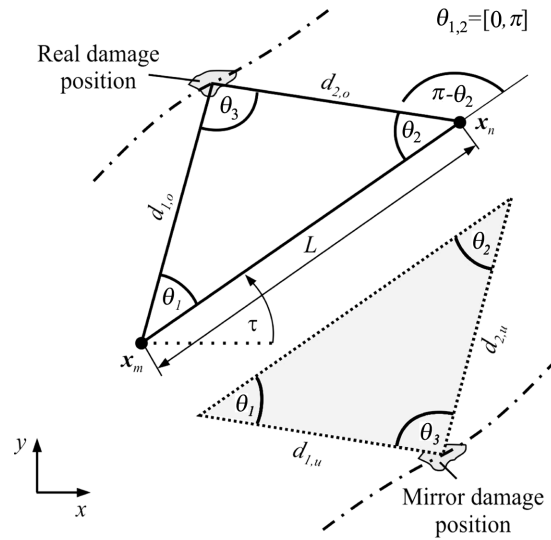

Fig. 6 Schematic to develop equations for damage localization in anisotropic plate-like structures

$$\frac{\sin(\theta_1)}{TOF_2 \cdot c_{Gr}(fd, \pi - \theta_2 + \tau, EOC)} = \frac{\sin(\theta_3)}{L} \tag{13}$$

The fact that the time-of-flight information in the differential signal contains the sum-travel time *TOF* from the actuator across the damage to the sensor results in:

$$TOF = TOF_1 + TOF_2 \tag{14}$$

Rearranging Eqs. (12) and (13), inserting them into (14) yields the final solution for the upper triangle

$$TOF \cdot \sin(\pi - \theta_1 - \theta_2) = \frac{L \sin(\theta_2)}{c_{Gr}(fd, \theta_1 + \tau, EOC)} + \frac{L \sin(\theta_1)}{c_{Gr}(fd, \pi - \theta_2 + \tau, EOC)} \tag{15}$$

This transcendental equation contains two variables θ_1 and θ_2 and cannot be solved analytically. The parameter τ denotes the angle between the horizontal axis and the connecting line between actuator *m* and sensor *n*. Therefore, it is transferred to an error function J_1, where the zeros are found numerically using standard routines like the Newton or gradient method

$$J_1 = TOF \cdot \sin(\pi - \theta_1 - \theta_2) - \frac{L \sin(\theta_2)}{c_{Gr}(fd, \theta_1 + \tau, EOC)} - \frac{L \sin(\theta_1)}{c_{Gr}(fd, \pi - \theta_2 + \tau, EOC)} \tag{16}$$

It can be concluded from this equation that the wave travels partly in the direction of θ_1 with the velocity $c_{Gr}(fd, \theta_1 + \tau, EOC)$ and partly in the direction of θ_2 with $c_{Gr}(fd, \pi - \theta_2 + \tau, EOC)$. In analogy to the upper triangle the error function for the lower triangle is

$$J_2 = TOF \cdot \sin(\pi - \theta_1 - \theta_2) - \frac{L \sin(\theta_2)}{c_{Gr}(fd, -\theta_1 + \tau, EOC)} - \frac{L \sin(\theta_1)}{c_{Gr}(fd, \pi + \theta_2 + \tau, EOC)} \tag{17}$$

Due to symmetry conditions infinite solutions for the damage position exist on both sides of the actuator-sensor pair (see Fig. 6). As a result of this ambiguity the damage potentially occurs on the one side or the other. The incorrect solution is called mirror damage position. In contrast to imaging strategies, this algorithm is not able to assume a certain pixel position to determine the propagation
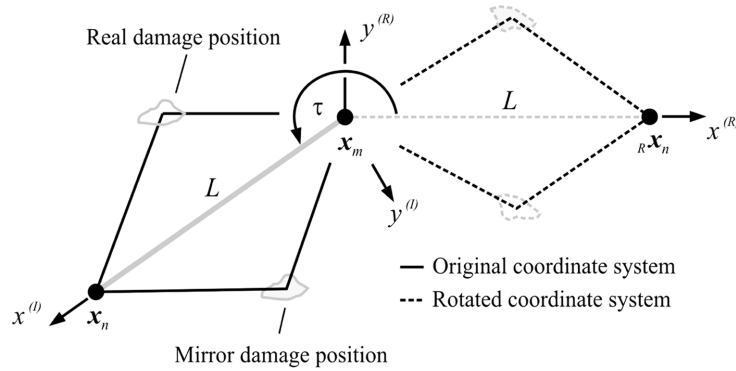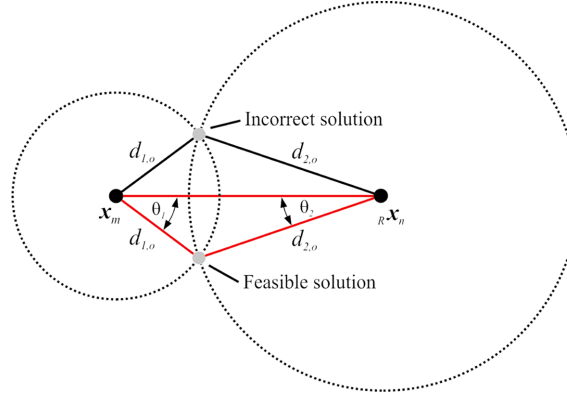

Fig. 7 Coordinate transform to simplify the interpretation of the geometric relations

Fig. 8 Intersection of two circles with the radii $d_{1,o}$ and $d_{1,u}$

rates in θ_1- and θ_2-direction. These rates are a product of solving the above equations and make the implementation much more complicated.

3.1.1 Numerical implementation

The following part demonstrates one possible implementation strategy to solve the error functions presented in Eqs. (16) and (17) (Moll 2011). The explanations solely focus on the solution of Eq. (16), which corresponds to the upper triangle of Fig. 6, because the implementation strategy is the same for both error functions. The first step is to extract the onset-times for all possible differential signals with e.g., a thresholding technique (Seydel and Chang 2001) or an energy-based algorithm (Grosse and Reinhardt 1999). Due to the complex geometric conditions it is helpful to perform a coordinate transform with respect to the original coordinate system $x^{(I)}$-$y^{(I)}$, see Fig. 7. Now, the actuator x_m is always on the left side of the rotated sensor position $_R x_n$.

For the solution of Eqs. (16) either θ_1 or θ_2 needs be fixed a priori in order to calculate the corresponding counterpart. This can be done by altering the value of θ_1 in equidistant steps of $\Delta\theta_1$ in the interval $[0,\pi]$ and solving the equation for θ_2. An accurate solution requires the interpolation of the wave velocities that are often available in form of look-up tables. Knowing the values of θ_1 and θ_2 enables the calculation of $d_{1,o}$ and $d_{2,o}$, see Eqs. (8) and (9). A feasible solution exists at the connecting points of $d_{1,o}$ and $d_{2,o}$. This is the problem of two intersecting circles with the radii $d_{1,o}$ and $d_{2,o}$. Generally, two solutions exist one at each side of the actuator-sensor path, see Fig. 8.
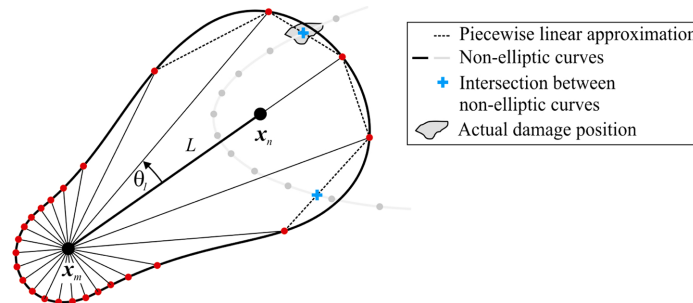
Fig. 9 Equidistant discretization of θ_1 with a step size of $\Delta\theta_1=\pi/12$ leads to curve segments with different lengths

It is important to underline that only one of these two solutions is feasible. For the upper triangle of Fig. 6 the feasible solution occurs on the right side of the actuator-sensor path, because the corresponding equation is only valid here. In analogy, the feasible solution for the lower triangle appears on the left side of this actuator-sensor path, because Eq. (17) is only valid there. The circle intersection problem must be solved for every value of θ_1. As a result, one attains a closed curve that has an elliptic form for an isotropic and a non-elliptic form for an anisotropic structure. The term non-elliptic highlights the difference to the classical ellipse method in (Tua *et al*. 2004). In a final step, the non-elliptic curve is transformed to its original coordinate system by the rotation of τ. It can happen that an equidistant discretization of θ_1 leads to an inhomogeneous distribution of the sampling points on the non-elliptic curve, see Fig. 9. Thus, the resulting segments have different lengths, that cause errors in regions with a coarse sampling and a high curvature. This error can be avoided when $\Delta\theta_1$ is small.

A well-defined localization of the damage requires more than one actuator-sensor pair. The non-elliptic curves intersect at the damage position. In order to automatically identify the curve intersections, the closed curve is discretized into piecewise linear parts. Here, a feasible solution is constrained by the interval of adjacent points and the geometry of the structure. Thus, a map of intersections occurs where the highest concentration of the points arise at the damage location. The point density is sparse in all the other places of the plate. Intersections outside the boundaries are neglected because they are beyond the feasible region. It is easy to see, that the computational demand is proportional to the resolution of the non-elliptic curves. A possible way to extract the regions with the highest point concentration is to apply a two-dimensional probability density function. In this paper, histogram-based estimation is used (Walters-Williams and Li 2009). This density function has one or more maxima, each corresponding to a damage position.

3.2 Imaging with the time-of-arrival algorithm

Imaging structural damages with the classical time-of-arrival algorithm requires a spatial discretization of the structure. That means that the coordinates of the pixel positions $P(x,y)$ and $\overline{P}(x,y)$ become available, see Fig. 10. Consequently, the intensity at $P(x,y)$ can be expressed as

$$I_P(x,y) = \sum_{m=1}^{n_T-1} \sum_{n=m+1}^{n_T} e_{mn}(t_{mn}(x,y)) \tag{18}$$

Where n_T denotes the number of transducers and $e_{mn}(t)$ the differential signal between actuator m and sensor n. The indices m and n account for the modified common source data acquisition technique. If $e_{mn}(t)$ is the differenced signal from the transducer pair m-n, then $e_{mn}(t_{mn}(x,y))$ shown in Fig. 11 corresponds to the sensor voltage of the signal scattered from the point (x,y). Hence, the highest intensity of the damage map occurs at the damage position. For the upper triangle in Fig. 10 the travel time is defined as

$$t_{mn}(x,y) = \frac{d_{1,o}}{c_{Gr}(fd, \theta_1 + \tau, EOC)} + \frac{d_{2,o}}{c_{Gr}(fd, \pi - \theta_2 + \tau, EOC)} \tag{19}$$

In analogy, the travel time for the lower triangle is

$$t_{mn}(x,y) = \frac{d_{1,u}}{c_{Gr}(fd, -\theta_1 + \tau, EOC)} + \frac{d_{2,u}}{c_{Gr}(fd, \pi + \theta_2 + \tau, EOC)} \tag{20}$$
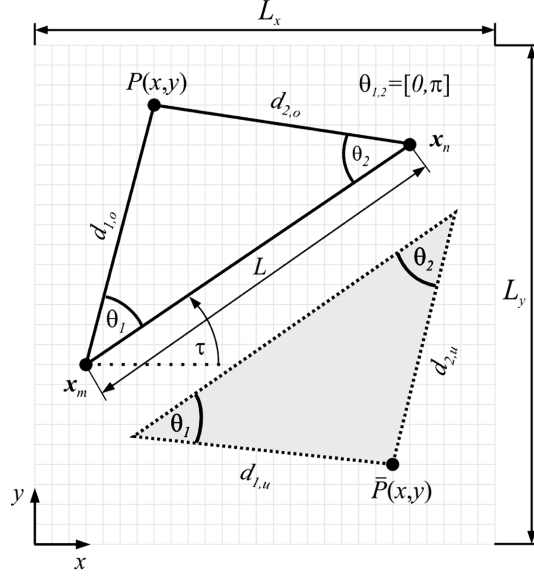
Fig. 10 Imaging with the time-of-arrival algorithm. The underlying spatial discretization is realized with equidistant sampling
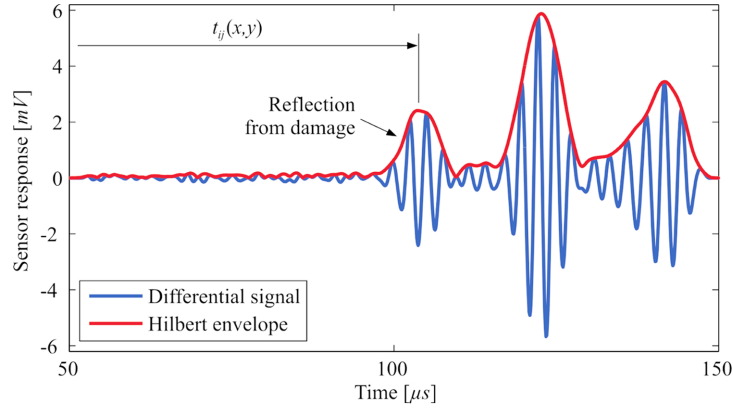

Fig. 11 Differential signal between measurements from the undamaged and damaged structure

In these equations $d_{1,o}$, $d_{2,o}$, $d_{1,o}$ and $d_{2,u}$ denote the Euclidean distances from the triangles of Fig. 10. The group velocity c_{Gr} is still a function of frequency f, the thickness of the structure d, the direction of propagation θ_1, θ_2 and τ as well as changing environmental and operational conditions *EOC*. It is easy to see from the above Eqs. (19) and (20) that they follow the mathematical description from the anisotropic triangulation methodology. On the other hand, there are several structural differences between the algorithms that will be discussed in the next section.

3.3 Discussion of the differences between the localization approaches

The main difference between the two localization techniques is the fact that the imaging approach with the TOA-algorithm requires an efficient spatial discretization of the structure in order to

determine the corresponding intensity value at these positions. A common strategy for this task is to use a grid approach where the spatial sampling points have an equidistant spacing. The grid approach causes a critical processing time for a high resolution damage map. Hence, a new technique has been developed recently that is based on design of experiments (Hartmann *et al.* 2011). Here, the *virtual measurement points* are placed adaptively in regions with high process nonlinearities that typically occur at the damage position.

Another difference is the way how the damage position is extracted. The triangulation approach determines a non-elliptic curve for each actuator-sensor pair. The intersections between all the non-elliptic curves lead to a point-cloud with the highest concentration at the damage position. If there is more then one damage, multiple point-clouds will occur each representing a structural defect, compare Fig. 14(a). The evaluation of the point-cloud is subsequently performed by a two-dimensional probability density function where the highest probability indicates the damage location. On the other hand the TOA-algorithm determines an image for each actuator-sensor pair. The application of suitable data fusion schemes, e.g., summation (Michaels *et al.* 2008), multiplication (Malinowski *et al.* 2007) or boolean operators (Su *et al.* 2009), merge the individual images to a final damage map, compare Fig. 15(a). Independent of the respective data fusion scheme, the damage location is always represented by the highest intensity.

A third difference refers to the fact that the triangulation algorithm requires a method that estimates the onset-time t_0 of the first wave packet in the differential signal accurately and autonomously. The quality of this *TOF*-information determines the performance of the overall damage localization, see Eqs. (16) and (17). Such an algorithm is less important for the imaging method. Knowing the onset-time t_0 improves the image quality in such a way, that secondary reflections in the differential signal are weighted with an exponential window $w(t)$ where $w(t=t_0)=1$, see Fig. 11 and (Michaels 2008). Since the triangulation algorithm normally uses the radiofrequency signal for the *TOF*-estimation directly, the imaging algorithm processes the envelope-detected or deconvolved differential signals in order to avoid local destructive interferences in the images (Michaels and Michaels 2006, Moll and Fritzen 2010, Moll *et al.* 2010).

Both approaches have in common that they assume a certain wave mode. A way to identify the wave modes inside an A-Scan is documented in (Li *et al.* 2009, Torres-Arredondo and Fritzen 2011). They exploit the physical property that the slope of the fundamental A_0 mode in the dispersion diagram is positive and the slope of the S_0 mode negative. Results were shown for isotropic and anisotropic structures.

4. Damage localization results

In order to validate the modeling approach and the localization techniques a case study has been conducted on a unidirectional glass-fibre reinforced plastic (GFRP) plate. A single-layered specimen was selected because of its highly anisotropic character. Fig. 12 shows the structure that has the dimensions 800 × 800 mm and a thickness of approximately 1.5 mm.

The fibres are oriented in y-direction. Nine piezoelectric transducers are attached to the surface of the structure with equidistant spacing. The circular piezo patches have a diameter of 10 mm and a thickness of 0.25 mm (Moll *et al.* 2012). In this study, the spectral element method is used to simulate the wave propagation (Schulte *et al.* 2010). Therefore, the plate is meshed with 6868 spectral shell elements using 36 nodes per element. A comparison between simulated and experimentally
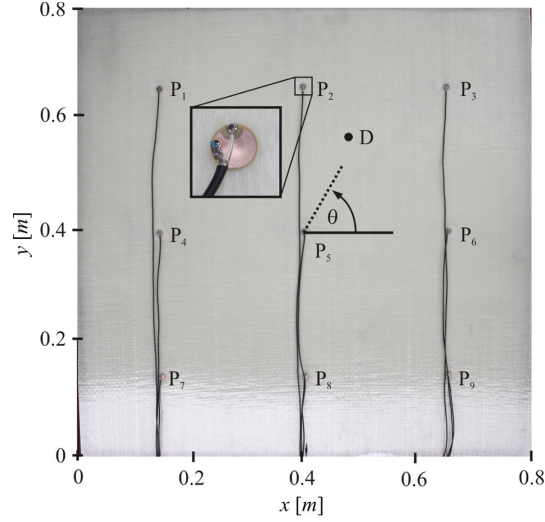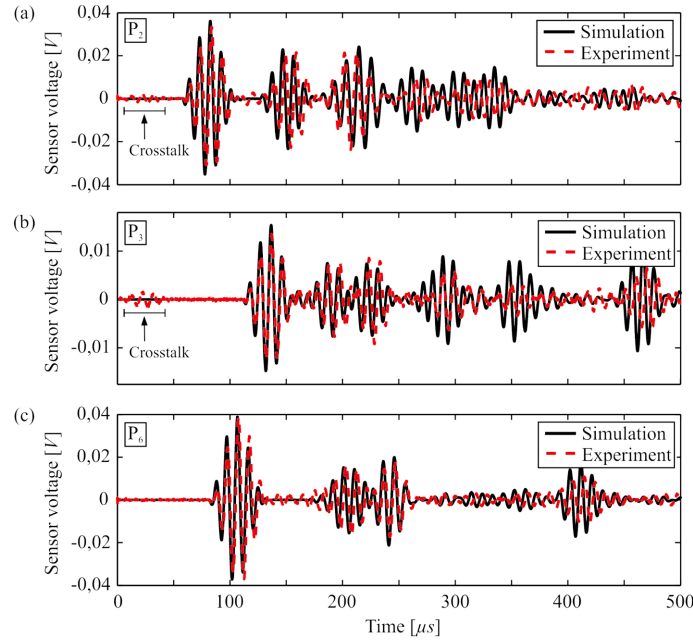
Fig. 12 GFRP plate with nine piezoelectric patches

Fig. 13 Simulated and measured sensor signals for P_2, P_3 and P_6; excitation at 100 kHz

measured signals, where the patch located in the center P_5 works as actuator, is shown in Fig. 13. A good agreement can be found in terms of arrival times and amplitudes of the wave packets.

To consider a well-defined point-like scatterer the simulation is used to generate ultrasonic signals for the undamaged and damaged structure. Here, a 3-cycle Hann-windowed toneburst is applied with a center frequency of 100 kHz. Actually, this is the same sensor configuration like in the experimental case. In simulation, damage is generated by a stiffness reduction of a single 12×12 mm element by 20%. As mentioned earlier, ultrasonic signals are recorded for the pristine and damaged

structure through the modified common source technique. Here, the symmetry is exploited that the information for actuator-sensor pair *n-m* is the same as for the actuator-sensor pair *m-n*. Thus, there are $n_T(n_T$-1$)/2$ possible combinations resulting in 36 signals.

The following analysis of damage localization is based on the group velocity characteristic that are theoretically calculated using the global matrix method. Fig. 14 shows the localization results using the triangulation method. The workflow to get the map of intersections follows the description of section 3.1. It can be observed in Fig. 14(a) that the highest intersection concentration occurs at the damage position. According to the mirror damage effect many scattered points occur at other regions of the plate. This is an inherent property of the algorithm that cannot be avoided. The two-dimensional probability density function, illustrated in Fig. 14(b), shows automatically the highest probability at the damage position. The absolute error between real and estimated damage location amounts 1.4 cm, which is a relative error with respect to the edges of the plate of 1.8%.

Damage visualization with the TOA-algorithm generates a single image for each actuator-sensor pair. Summing all individual images forms the final damage map as shown in Fig. 15(a). The localization results for the unidirectional composite plate is shown in Fig. 15(b), where the highest intensity of the damage map estimates the damage position. The absolute error between the point of maximum intensity and the real damage position is 1.1 cm. This is a relative error with respect to
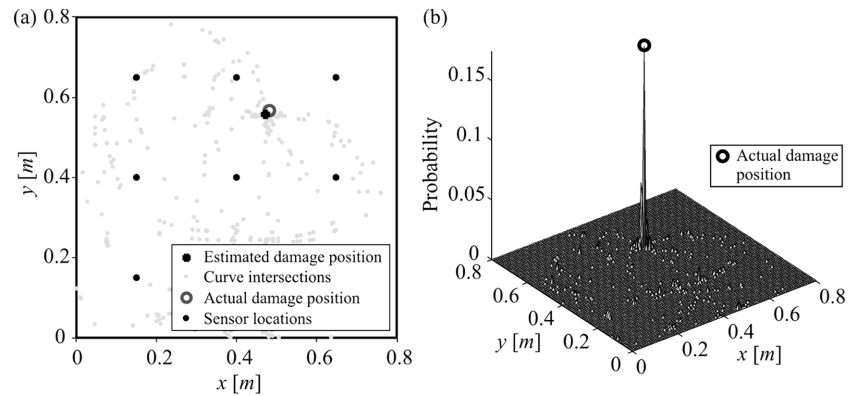

Fig. 14 (a) Map of intersections as a result of nonlinear curve analysis and (b) two-dimensional probability density function
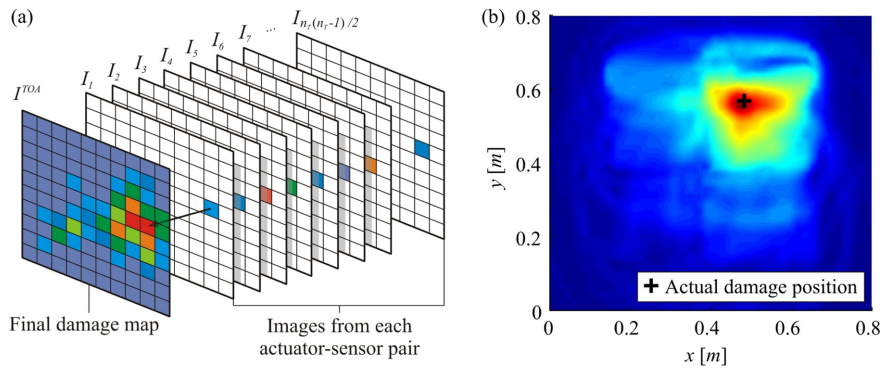

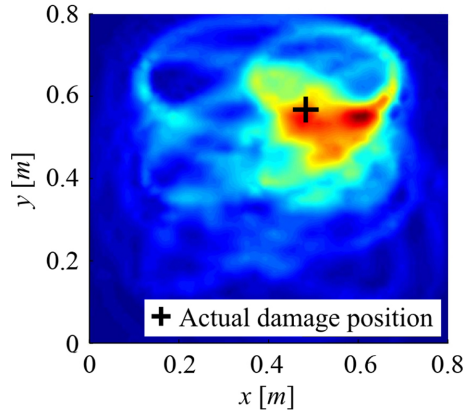Fig. 15 (a) Visualization of the data fusion process and (b) final damage map for the TOA-algorithm

Fig. 16 Replacing the anisotropic wave curve with the constant mean velocity causes a localization error for
the TOA-algorithm of 11.9 mm, i.e., 14.8%, with respect to the edges of the structure. This
demonstrates the importance to incorporate the anisotropic wave curve into the localization routines

the edges of the plate of 1.4%. Fig. 16 shows the effect when the anisotropic velocity is replaced in the analysis by means of the constant mean velocity. This causes severe localization errors of 11.9 cm, i.e., 14.8%, for damage imaging. In case of the triangulation approach the error associated with the homogenization is 2.7 cm, i.e., 3.3%.

5. Conclusions

This paper described computational aspects of damage localization in anisotropic structures. The first part provides an overview of the modeling of Lamb wave propagation in composite materials focussing on the numerical implementation of the well-known global matrix method. Here, the complex three-dimensional elasticity equations are transferred to a quadratic eigenvalue problem. Subsequently, the global matrix is assembled based on stress and displacement relations obtained by substitution of the previously calculated eigenvalues, and its determinant leads to a characteristic function relating angular frequency to wavenumber. The angular-dependent dispersion curves are a product of the proposed automatic tracing procedure. The dispersion curves for the fundamental modes of propagation are presented and analyzed in order to depict the wave propagation behaviour in anisotropic plates. A validation of the wave velocity characteristic has been performed with experimental time-delay measurements from a single-layered and a multi-layered composite structure.

In the second part two localization algorithms have been presented that are able to identify the damage position in anisotropic structures. Both localization routines essentially require the directional wave velocity characteristic of the fundamental wave modes that is calculated here by the global matrix method. The localization methodologies are compared in terms of their individual algorithmic properties. Results were shown for the same unidirectional composite structure as mentioned above using simulated time-traces from the spectral element method. It can be concluded that both localization methodologies locate the damage position accurately. Moreover, it was shown that significant localization errors occur as soon as the inhomogeneous anisotropic velocity characteristic was replaced by the corresponding constant mean velocity.

Future investigations will focus on the experimental validation of the proposed localization

techniques. A general issue for the differential approach is to get highly synchronized measurements in order to avoid false onset-time estimations that can lead to localization errors. Another interesting aspect is to study the localization performance considering different types of damages, like e.g., various types of delaminations (that differ in size and shape) and corrosion damages as well as structures with a more complex geometry.

Acknowledgements

References

Auld, B.A. (1973), *Acoustic Fields and Waves in Solids*, Wiley-Interscience, New York.

Barkanov, E., Chate, A., Rucevskis, S. and Skukis, E. (2007), "Characterisation of composite material properties by an inverse technique", *Key Eng. Mater.*, **345-346**(1), 1319-1322.

Calomfirescu, M. and Herrmann, A.S. (2007), "On the propagation of lamb waves in viscoelastic composites for shm applications", *Key Eng. Mater.*, **347**(1), 543-548.

Castaings, M. Hosten, B. and Kundu, T. (2000), "Inversion of ultrasonic, plane-wave transmission data in composite plates to infer viscoelastic material properties", *NDT & E. Int.*, **33**(6), 377-392.

Clarke, T. Simonetti, F. and Cawley, P. (2010), "Guided wave health monitoring of complex structures by sparse array systems: influence of temperature changes on performance", *J. Sound Vib.*, **329**(12), 2306-2322.

Croxford, A.J., Moll, J., Wilcox, P.D. and Michaels, J.E. (2010), "Efficient temperature compensation strategies for guided wave structural health monitoring", *Ultrasonics*, **50**(4-5), 517-528.

Davies, J., Simonetti, F., Lowe, M. and Cawley, P. (2006), "Review of synthetically focused guided wave imaging techniques with application to defect sizing", *Proceedings of the European Conference on Nondestructive Testing*, Berlin, Deutschland, NDT.net, 142-149.

Grosse, C.U. and Reinhardt, H.W. (1999), "Schallemissionsquellen automatisch lokalisieren - entwicklung eines algorithmus", *Materialprüfung*, **41**(9), 342-347.

Hartmann, B., Moll, J., Nelles, O. and Fritzen, C.P. (2010), "Modeling of nonlinear wave velocity characteristics in a structural health monitoring system", *Proceedings of the IEEE Multi-Conference on Systems and Control*, Tokyo Bay, Japan, 1011-1016.

Hartmann, B., Moll, J., Nelles, O. and Fritzen, C.P. (2011), "Hierarchical local model trees for design of experiments in the framework of ultrasonic structural health monitoring", *Proceedings of the IEEE Multi-Conference on Systems and Control*, Denver, USA, 1163-1170.

Hayashi, T. and Kawashima, K. (2002), "Multiple reflections of lamb waves at a delamination", *Ultrasonics*, **40**(1-8), 193-197.

Hearn, E.J. (1977), *Mechanics of materials: An introduction to the mechanics of elastic and plastic deformation of solids and structural components*, International Series on Materials Science and Technology, 1st Ed.

Konstantinidis, G., Drinkwater, B.W. and Wilcox, P.D. (2006), "The temperature stability of guided wave structural health monitoring systems", *Smart Mater. Struct.*, **15**(4), 967-976.

Kundu, T. (2004), *Ultrasonic Nondestructive Evaluation: Engineering and Biological Material Characterization*, London, CRC Press.

Li, F., Meng, G., Ye, L. and Kageyama, K. (2009), "Dispersion analysis of lamb waves and damage detection for aluminum structures using ridge in the time-scale domain", *Measurement Sci. Tech.*, **20**(9).

Lowe, M.J.S. (1993), *Plate waves for the NDT of diffusion bonded titanium. Imperial College of Science, Technology and Medicine*, London.

Lowe, M.J.S. (1995), "Matrix techniques for modeling ultrasonic waves in multilayered media", *IEEE T. Ultrason. Ferr.*, **42**(4), 525-542.

Lu, Y. and Michaels, J.E. (2005), "A methodology for structural health monitoring with diffuse ultrasonic waves in the presence of temperature variations", *Ultrasonics*, **43**(9), 717-731.

Malinowski, P., Wandowski, T., Trendafilova, I. and Ostachowicz, W. (2007), "Multi-phased array for damage localisation", *Key Eng. Mater.*, **347**, 77-82.

Mal, A.K. (1988), "Wave propagation in layered composite laminates under periodic surface loads", *Wave Motion*, **10**, 257-266.

Michaels, J.E., Croxford, A.J. and Wilcox, P.D. (2008), "Imaging algorithms for locating damage via in situ ultrasonic sensors", *Proceedings of the IEEE Sensor Application Symposium*, Atlanta, USA, 63-67.

Michaels, J.E. and Michaels, T.E. (2006), "Enhanced differential methods for guided wave phased array imaging using spatially distributed piezoelectric transducers", *Proceedings of the Review of Progress in Quantitative Nondestructive Evaluation*, Portland, USA, American Institute of Physics, 837-844.

Moll, J. and Fritzen, C.P. (2010), "Time-varying inverse filtering for high resolution imaging with ultrasonic guided waves", *Proceedings of the 10th European Conference on Non-Destructive Testing*, Moscow, Russia (on CD-ROM).

Moll, J. and Fritzen, C.P. (2012), "Guided waves for autonomous online identification of structural defects under ambient temperature variations", *J. Sound Vib.*, **331**(20), 4587-4597.

Moll, J., Golub, M.,Glushkov, E., Glushkova, N. and Fritzen, C.P. (2012), "Non-axisymmetric lamb wave excitation by piezoelectric wafer active sensors", *Sens. Actuat. A. Phys.*, **174**, 173-180.

Moll, J., Heftrich, C. and Fritzen, C.P. (2011), "Time-varying inverse filtering of narrowband ultrasonic signals", *Struct. Health Monit.,* **10**(4), 403-415.

Moll, J., Schulte, R.T. Hartmann, B., Fritzen, C.P. and Nelles, O. (2010), "Multi-site damage localization in anisotropic plate-like structures using an active guided wave structural health monitoring system", *Smart Mater. Struct.*, **19**(4).

Moll, J. (2011), *Strukturdiagnose mit Ultraschallwellen durch Verwendung von piezoelektrischen Sensoren und Aktoren*, PhD thesis, University of Siegen, Germany, Schriftenreihe der Arbeitsgruppe fuer Technische Mechanik im Institut fuer Mechanik und Regelungstechnik - Mechatronik, Publisher: Claus-Peter Fritzen, ISSN 2191-5601.

Nayfeh, A.H. (1991), "The general problem of elastic wave propagation in multilayered anisotropic media", *J. Acoust. Soc. Am.*, **89**(4),1521-1531.

Nayfeh, A.H. (1995), "Wave propagation in layered anisotropic media with applications to composites", *Appl. Math. Mech.*, **39**.

Ng, C.T. and Veidt, M. (2009), "A lamb-wave-based technique for damage detection in composite laminates", *Smart Mater. Struct.*, **18**(7).

Pavlakovic, B. (1997), "Disperse: a general purpose program for creating dispersion curves", In: Review of Progress in Quantitative Nondestructive Evaluation, 185-192..

Rose, J.L. (1999), *Ultrasonic Waves in Solid Media*, Cambridge University Press.

Schulte, R.T., Fritzen, C.P. and Moll, J. (2010), "Spectral element modelling of wave propagation in isotropic and anisotropic shell-structures including different types of damage", *Mater. Sci. Eng.*, **10**(1).

Schulte, R.T. (2010), *Modellierung und simulation von wellenbasierten structural health monitoring-systemen auf basis von spektralelementen*, PhD thesis, University of Siegen, Germany, Schriftenreihe der Arbeitsgruppe fuer Technische Mechanik im Institut fuer Mechanik und Regelungstechnik - Mechatronik, Publisher: Claus-Peter Fritzen.

Seydel, R. and Chang, F.K. (2001), "Impact identification of stiffened composite panels i. system development", *Smart Mater. Struct.*, **10**(2), 354-369.

Staszewski, W., Boller, C. and Tomlinson, G.R. (2004), *Health monitoring of Aerospace structures: smart sensor technologies and signal processing*, Wiley.

Su, Z., Wang, X., Cheng, L., Yu, L. and Chen, Z. (2009), "On selection of data fusion schemes for structural damage evaluation", *Struct.Health Monit.*, **8**(3), 223-241.

Szabo, J. and Wu, T.L. (2000), "A model for longitudinal and shear wave propagation in viscoelastic media", *J. Acoust. Soc. Am.*, **107**(5), 2437-2446.

Tisseur, K. and Meerbergen, F. (2001), "The quadratic eigenvalue problem", *SIAM Rev.*, **43**(2), 235-286.

Torres-Arredondo, M.A. and Fritzen, C.P. (2011), "Characterization and classification of modes in acoustic emission based on dispersion features and energy distribution analysis", *Proceedings of the ICEDyn* ,Tavira, Portugal (on CD-ROM).

Torres-Arredondo, M.A. and Fritzen, C.P. (2011), *A viscoelastic plate theory for the fast modelling of lamb wave solutions in ndt/shm applications*, In: NDT-E of Composite Materials - CompNDT, Available Online: NDT.net.

Torres-Arredondo, M.A. and Fritzen, C.P. (2012), "Ultrasonic guided wave dispersive characteristics in composite structures under variable temperature and operational conditions", *Proceedings of the 6th European Workshop in Structural Health Monitoring*, Berlin, Germany.

Tua, P.S. Quek, S.T. and Wang, Q. (2004), "Detection of cracks in plates using piezo-actuated lamb waves", *Smart Mater. Struct.*, **13**(4), 643-660.

Vasiliev, E.V. and Morozov, V.V. (2007), *Advanced mechanics of composite materials*, Elsevier Ltd.

Walters-Williams, J. and Li, Y. (2009), "Estimation of mutual information: a survey", *Proceedings of the4th International Conference on Rough Set and Knowledge Technology*, Gold Coast, Australia, 389-396.

Wang, Y. and Yuan, F.G. (2007), "Group velocity and characteristic wave curves of lamb waves in composites: Modeling and experiments", *Compos. Sci. Technol.*, **67**(7-8), 1370-1384.

Whitney, J.M. and Sun, C.T. (1973), "A higher order theory for extensional motion of laminated composites", *J. Sound Vib.*, **30**(1), 85-97.

Yu, L., Giurgiutiu, V. and Pollock, V. (2008), "A multi-mode sensing system for corrosion detection using piezoelectric wafer active sensors", *Proceedings of the SPIE (Sensors and Smart Structures Technologies for Civil, Mechanical, and Aerospace Systems)*, San Diego, USA, 69322H(1-12).

CC

Appendix A

Combining the equations of motion (1) with the strain-stress (2) and strain-displacement relations (3), and substituting (4) leads to a quadratic eigenvalue relation in terms of p that can be written as

$$(Ap^2 + Bp + D)U = 0 \tag{21}$$

where **A** and **D** are 3×3 symmetric matrices and **B** is a 3×3 self-adjoint matrix, whose non-zero elements are given as

$$A_{11} = C_{55}, A_{12} = C_{45}, A_{22} = C_{44}, A_{33} = C_{33} \tag{22}$$

$$B_{13} = -i[(C_{13} + C_{55})\cos(\theta) + (C_{36} + C_{45})\sin(\theta)] \tag{23}$$

$$B_{23} = -i[(C_{36} + C_{45})\cos(\theta) + (C_{23} + C_{44})\sin(\theta)] \tag{24}$$

$$D_{11} = C_{11}\cos^2(\theta) + 2C_{16}\cos(\theta)\sin(\theta) + C_{66}\sin^2(\theta) - \rho c_{ph}^2 \tag{25}$$

$$D_{12} = C_{16}\cos^2(\theta) + (C_{12} + C_{66})\cos(\theta)\sin(\theta) + C_{26}\sin^2(\theta) \tag{26}$$

$$D_{22} = C_{55}\cos^2(\theta) + 2C_{45}\cos(\theta)\sin(\theta) + C_{44}\sin^2(\theta) - \rho c_{ph}^2 \tag{27}$$

$$D_{33} = C_{55}\cos^2(\theta) + 2C_{45}\cos(\theta)\sin(\theta) + C_{44}\sin^2(\theta) - \rho c_{ph}^2 \tag{28}$$

A survey into the quadratic eigenvalue problem, treating its mathematical properties and a variety of numerical solution techniques can be found in Tisseur and Meerbergen [40]. Eigenvalue solutions occur in three pairs related to each other by a change of sign, one or more of which can be imaginary. In a next step, the displacement vector can be normalized without loss of generality by any of the displacement components, e.g. U_{1q}. Using the relations (21) for each previously calculated p_q, $q=1,2,...,6$, one can express the displacement ratios $V_q = U_{2q}/U_{1q}$ and $W_q = U_{3q}/U_{1q}$ as

$$V_q = \frac{(D_{11} + A_{11}p_q^2)B_{23} - (D_{12} + A_{12}p_q^2)B_{13}}{(D_{22} + A_{22}p_q^2)B_{13} - (D_{12} + A_{12}p_q^2)B_{23}} \tag{29}$$

$$W_q = \frac{p_q[(D_{11} + A_{11}p_q^2)B_{23} - (D_{12} + A_{12}p_q^2)B_{13}]}{(D_{16} + A_{12}p_q^2)(D_{33} + A_{33}p_q^2) - B_{23}B_{13}p_q^2} \tag{30}$$

Combining the Eq. (22) to (28) and (29) to (30) with the stress-strain (2) and strain-displacement (3) relations, and using linear superposition of harmonic functions, the formal solutions for the displacements and stresses can be expressed in a matrix form **K** as depicted below

$$\begin{bmatrix} u_1 \\ u_2 \\ u_3 \\ u_{33} \\ u_{13} \\ u_{23} \end{bmatrix} = \begin{bmatrix} 1 & 1 & 1 & 1 & 1 & 1 \\ V_1 & V_2 & V_3 & V_4 & V_5 & V_6 \\ W_1 & W_2 & W_3 & W_4 & W_5 & W_6 \\ R_{11} & R_{12} & \boldsymbol{K}_{13} & R_{14} & R_{15} & R_{16} \\ R_{21} & R_{22} & R_{23} & R_{24} & R_{25} & R_{26} \\ R_{31} & R_{32} & R_{33} & R_{34} & R_{35} & R_{36} \end{bmatrix} \begin{bmatrix} U_{11} \\ U_{12} \\ U_{13} \\ U_{14} \\ U_{15} \\ U_{16} \end{bmatrix} e^{ik(x_1\cos(\theta) + x_2\cos(\theta) + px_3 - c_{ph}^t)} \tag{31}$$

where

$$R_{1q} = C_{13}\cos(\theta) + C_{23}\sin(\theta)V_q - iC_{33}p_qW_q + C_{36}(\sin(\theta) + V_q\cos(\theta)) \tag{32}$$

$$R_{2q} = C_{44}(p_qV_q + W_q\sin(\theta)) + C_{45}(p_q + W_q\cos(\theta)) \tag{33}$$

$$R_{3q} = C_{45}(p_qV_q + W_q\sin(\theta)) + C_{55}(p_q + W_q\cos(\theta)) \tag{34}$$

The developed solution can be used now for the analysis of single and multilayered media since a general expression for the displacement and stress components has been derived. For a required solution, boundary and continuity conditions can be imposed.